3D-printed biocompatible hollow microneedle-based electrochemical sensor for wireless glucose monitoring

Chuchu Chen[1,†],Yonghao Fu[1,†], Yun Liu[2], Yuehe Lin[1], Dan Du[1,], Kaiyan Qiu[1,*]*

[1] School of Mechanical and Materials Engineering, Washington State University, Pullman, Washington 99164, United States

[2] Research School of Chemistry, Australian National University, Canberra, ACT 2601, Australia

* Corresponding authors.

† These authors contributed equally to this work.

E-mail: kaiyan.qiu@wsu.edu; annie.du@wsu.edu

Keywords: wearable electrochemical sensor; single-atom nanozyme; hollow microneedle array; wireless glucose monitoring; resin 3D printing

Abstract:

Wearable electrochemical sensors have aroused tremendous attention due to their great potential for *in situ* and continuous assessment for glucose monitoring. Conventional fingerstick test is the easiest and most efficient method for glucose evaluation, but invasive and painful. Here we introduce a wearable and user-friendly microneedle-based electrochemical sensor, fabricated via resin 3D printing and integration of a single-atom nanozyme-modified electrode, offering excellent biocompatibility, high sensitivity and superior selectivity for glucose monitoring. This minimally invasive electrochemical sensor demonstrates the capability to extract artificial interstitial fluid using biocompatible hollow microneedles and a finger-activated pump, enabling continuous monitoring of dynamic glucose concentration changes. This electrochemical sensor exhibits remarkable sensitivity and exceptional selectivity, with a linear range of 0.1 μM to 50 mM and a limit of detection of 0.059 μM, attributed to the incorporation of single-atom nanozymes with peroxidase-like enzymatic activity. The glucose concentration data are wirelessly transmitted to a mobile app in real time, offering user-friendly access and facilitating remote monitoring. The described electrochemical sensor presents the possibilities for point-of-care health monitoring applications.

1. Introduction

Diabetes is a widely spread chronic metabolic disorder [1, 2]. Glucose is the most important risk indicator of diabetes, and rigid glycemic control and continuous glucose monitoring have been proven remarkable to reduce the deterioration of diabetes and prevent secondary complications [3, 4]. Continuous glucose monitoring can provide accurate and reliable glucose measurements in real time [5, 6]. Traditional fingerstick glucose sensing is invasive and painful, inevitably causing damage to the skin if tested 6 to 8 times a day [7]. To address these challenges, various wearable noninvasive or minimally invasive sensors have emerged as promising alternatives for continuous glucose monitoring [8, 9]. These devices leverage advanced technologies such as optical [10, 11], thermal [12, 13], transdermal electrochemical techniques [14, 15], offering high versatility. Despite their potential, they still face limitations, including sensitivity, selectively, biocompatibility and user convenience [16].

Interstitial fluid (ISF) processes a similar composition profile as the blood due to its capability to exchange substances between the cells and the blood by diffusion [17, 18], making it a valuable candidate for glucose monitoring [19]. Despite promising, obtaining ISF is still challenged by miniscule volumes available in the dermis ($120\ \mu l/cm^2$) and the filtration effect caused by the applied force, leading to slow extraction rates for continuous sampling [20, 21]. Microneedles (MNs) have been used for drug delivery and transdermal extraction [22-24]. The length of the MNs is generally between 100 to 1000 μm, which can guarantee that microneedles can puncture the stratum corneum without stimulating the nerves and vessels in the dermis for painless and minimally invasive effects [19, 25]. Hollow microneedles (HMNs) have been reported to sample ISF via epidermis piercing and capillary force for glucose monitoring [26, 27]. To date, the combination of micropores and suction approach has improved the collection rate over sole needle-based extraction and reduced tissue damage caused by suction blisters [21, 28, 29].

Nanozymes, nanomaterials with enzyme-like activities, have been developed as efficient catalysts by researchers due to the advantages of low cost, ultrahigh activity, high stability and so on [30]. Single-atom nanozymes (SANs), a type of nanozyme characterized by atomically dispersed active sites, process ultrahigh enzyme-like activity and excellent chemical stability, endowing them with unique catalytic performance [31]. Recently, Fe-based SANs with dispersed Fe atoms, known as Fe-N-C-based SANs, have shown superior peroxidase-like characteristics [32]. The excellent catalytic performance of Fe-N-C SANs for H_2O_2 makes them widely used in various sensor

2

applications, such as the detection of glucose, uric acid, lactate, herbicide and butyrylcholinesterase, as reported in our previous studies [33-35].

Herein, we present a novel biocompatible wearable electrochemical sensor for glucose monitoring in ISF. Compared with previous glucose sensors, our study introduces an innovative combination of 3D-printed HMNs and SANs to address the key limitations in existing technologies. HMNs are fabricated by biocompatible resin, allowing minimally invasive sampling for ISF and ensuring safe interaction with the skin without irritation and toxicity concerns. The incorporation of SANs significantly boosts the sensitivity and selectivity of electrochemical sensing, offering a wide linear range of 0.1 µM to 40 mM for glucose. The integration of 3D-printed HMNs and a finger-activated pump demonstrates the ISF extraction capability in a biocompatible and minimally invasive approach, which is validated through the sampling of artificial ISF from skin-mimicking phantom gel "*in vivo*". Furthermore, the sensor is coupled with a potentiostat, enabling real-time and wireless data transmission to a smartphone app to provide immediate results of the glucose levels. Beyond glucose detection, this versatile platform holds great potential for expanding the detection of a wide range of biomarkers in ISF. This research aims to develop and validate the wireless sensor, showcasing its sensitivity and selectivity using a skin-mimicking phantom gel, thereby laying the foundation for future advancements in wearable biosensors.

2. Results and Discussion

2.1 Design of the 3D-printed microneedle-based electrochemical sensor

As illustrated in **Figure 1A**, the biocompatible 3D-printed microneedle-based electrochemical sensor includes three key components: 1) touch-activated pump to enhance fluid extraction, 2) SANs-functionalized screen-printed electrode (SPE) for *in situ* and real-time electrochemical glucose analysis, 3) 3D-printed hollow microneedle array for minimal invasive extraction of interstitial fluid. The flexible 3D-printed pump (inner chamber volume: 232.8 cm^3) is incorporated to create negative pressure by finger pressing to facilitate the sampling of interstitial fluid through the hollow microneedles and transport it to the surface of the sensing area. Once the finger load is removed, the pump can self-recover to the initial state. The working electrode (WE) of SPE chip is functionalized by SANs for sensitive detection of the glucose in the ISF. The SPE is stabilized between the pump and microneedle patch by epoxy adhesives. Two circular holes (1 mm in

diameter) are pre-punched between the electrodes, serving as channels to generate negative pressure inside the hollow microneedles. The fabrication process, as shown in **Figure 1B**, comprises three steps: 1) modify the WE of the SPE with SANs; 2) Punch two circular holes between three electrodes; 3) attach the HMNs and the pump with adhesives to both sides of the SPE. During measurement, the SPE is connected to a finger-size potentiostat, where the electrochemical signals are recorded as electric signals and wirelessly transmitted. The glucose concentration results are displayed on a smartphone app for real-time health monitoring.
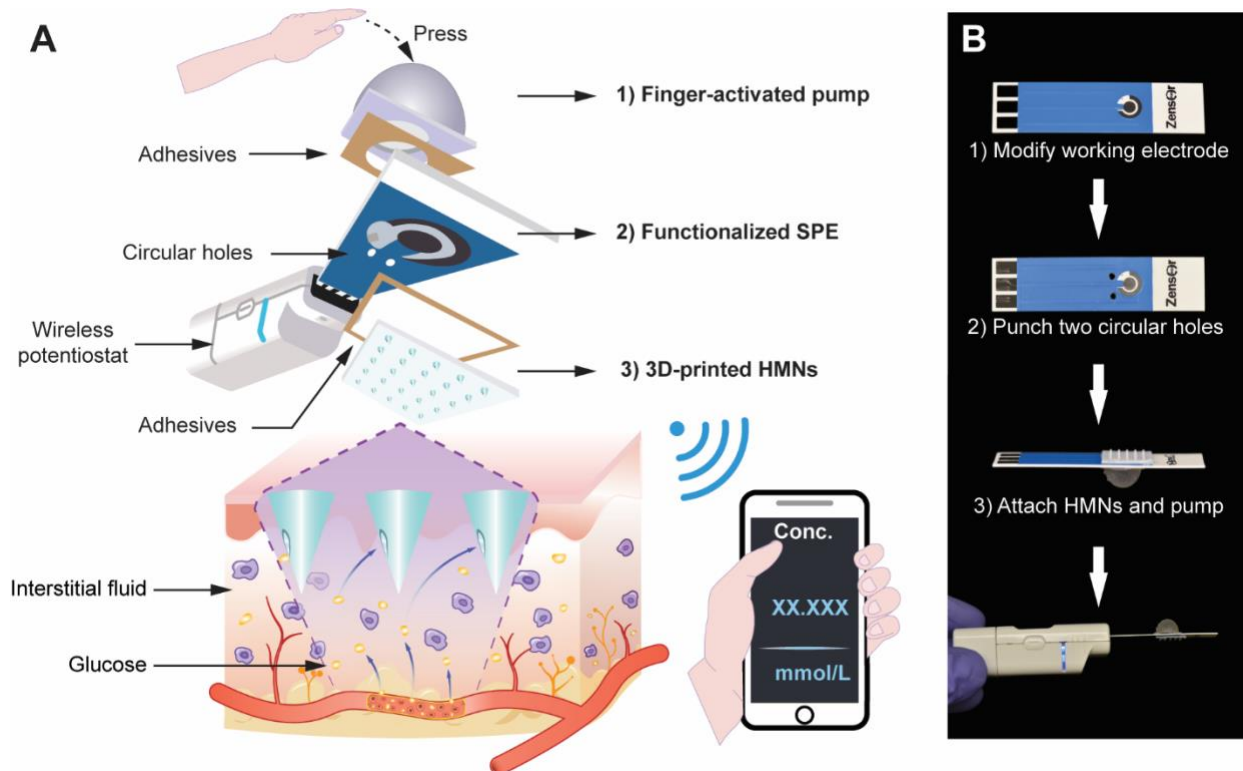

Figure 1. Concept of the 3D-printed microneedle-based electrochemical sensor. A) Schematic illustrating the exploded view of the sensor; B) Fabrication procedures of the integrated sensor.

2.2 Synthesis and characterization of Fe-N-C SANs

The preparation of Fe-N-C SANs was based on the previous reports [33, 36]. The synthesis schematic diagram is shown in **Figure S1**. Briefly, the zeolitic imidazolate framework-8 (ZIF-8), a class of metal-organic frameworks (MOFs), was synthesized from Zn $(NO_3)_2$ and 2-Methylimidazole. Then, the Fe $(NO_3)_3$-doped ZIF-8 was from Fe $(NO_3)_3$ and ZIF-8 as precursor (ZIF-8@Fe $(NO_3)_3$). The Fe-N-C SANs were obtained after pyrolysis at 900 °C. The transmission electron microscopy (TEM) image shows the characterization results of the Fe-N-C SANs (**Figure 2A**). Fe-N-C SANs

of similar shape and size (rhombic dodecahedral) were observed in the TEM images. **Figure S2** displays a high-angle annular dark-field scanning transmission electron microscope (HAADF-STEM) image. Bright dots are observed in images, representing dispersed Zn and Fe atoms. This phenomenon is attributed to the Z-contrast between metal and carbon. The single-atom feature of SANs, demonstrated by the dispersed Zn and Fe in HAADF-STEM image is key to their excellent peroxidase-like activity.

Cyclic voltammetry (CV) was used to evaluate the electrocatalytic performance of Fe-N-C SANs for H_2O_2. The Fe-N-C SANs were loaded onto SPE at a density of 0.1 mg cm^{-2}. The CV curves of bare SPE and Fe-N-C SANs-coated SPE in the presence and absence of 2.5 mM H_2O_2 in 0.01 M phosphate-buffered saline (PBS, pH 7.4) are shown in **Figure 2B**. The bare SPE exhibited a low current and weak response to H_2O_2, while Fe-N-C SANs-coated SPE showed a reduction peak at -0.1 V in PBS solution. Besides, the bare SPE showed a weak response at -0.64 V to 2.5 mM H_2O_2. The CV of SANs-coated SPE in PBS solution showed a reduction peak and significant reduction current at -0.1 V. This indicates that the catalytic effect of Fe-N-C SANs lowered the reduction peak of hydrogen peroxide reaction by 0.54 V, which significantly improves the sensitivity and selectivity of the sensor for H_2O_2 detection. **Figure S3** shows the CV curves of Fe-N-C SANs-coated SPE in PBS solution with 7.5, 5, and 2.5 mM H_2O_2. The CV curves showed an increasing reductive current (from –36.90 μA to –85.32 μA) as the increase of H_2O_2 concentration from 2.5 to 7.5 mM. The above result shows the excellent electrocatalytic ability of Fe-N-C SANs for H_2O_2 decomposition and demonstrates the relationship between response current and analyte concentration.

The continuous H_2O_2 detection is shown in **Figure S4**. **Figure S4A** shows the amperometry curve of Fe-N-C SANs during the continuous addition of H_2O_2 in PBS solution. With the addition of H_2O_2 solution, the response current increased gradually, which demonstrates the excellent catalytic performance of Fe-N-C SANs. The concentration of H_2O_2 in the system after adding H_2O_2 was recorded, and a linear relationship between H_2O_2 concentration and response current is shown in **Figure S4B**. The results indicate that the Fe-N-C SANs can be used for real-time and continuous detection for the concentration of H_2O_2 by electrochemical method and the extremely high R^2 value (0.998) also reflects the accuracy of the detection.

2.3 Detection performance of Fe-N-C SANs-coated SPE

The preparation process of the electrochemical glucose sensor is illustrated in **Figure 2**. As a portable electrochemical transducer, SPE is commonly used in the design of portable and convenient sensors [37, 38]. Glucose oxidase (GOx) catalyzes the oxidation of glucose, producing gluconolactone and releasing H_2O_2 [39]. Therefore, the SANs-functionalized glucose biosensor is capable of measuring glucose levels in samples by detecting the concentration of H_2O_2. In this study, Fe-N-C SANs are used for glucose sensing due to their excellent peroxidase-like activity and efficient catalytic performance for H_2O_2 detection, which was demonstrated by our previous [32, 33, 40-42]. GOx, a particular oxidoreductase, enables to use oxygen as an electron acceptor and oxidize the β-D-glucose to produce D-glucono-δ-lactone and release H_2O_2 [39]. The catalytic mechanism of GOx is as follows:

$$GOx (FADH_2) + O_2 \rightarrow GOx (FAD) + H_2O_2$$

$$Glucose + GOx (FAD) \rightarrow GOx (FADH_2) + Gluconolactone$$
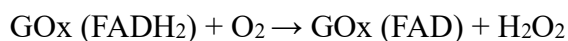
As a result, due to the excellent peroxidase-like activity of Fe-N-C SANs, reduction of H_2O_2 in electrode surface are enhanced dramatically, leading to high response current at a low overpotential. This study combined Fe-N-C SANs and GOx as sensing elements and SPE to fabricate this SPE-based electrochemical detection platform. The electrochemical response of the sensor to glucose was measured by the CV method in the electrochemical workstation. The CV curves of bare SPE, GOx-coated SPE and SANs-GOx-coated SPE are displayed in **Figure 2C**. No redox peak for bare SPE without SANs and GOx. Compared with the SPE with only GOx added, significant response peaks were observed for the SPE with SANs and GOx, indicating that the modification on SPE improves the electrochemical process and enhances electrochemical signals. The comparison of glucose detection performance between SANs/GOx-coated SPE and GOx-coated SPE is shown in **Figure 2D**. The higher slope of the SANs/GOx-coated SPE demonstrates that SANs can enhance the sensitivity and accuracy of glucose detection. In **Figure 2E**, amperometry measurement was conducted on electrode for the detection of glucose at -0.22 V in PBS (0.1 M, pH = 7.4). The detection range of glucose sensing is from 0.1 μM to 50 mM, where a linear relationship between the concentration of glucose and responding current is observed from 0.1 mM to 40 mM with the equation $Y = 6.66*X + 86.8$ and an R^2 value of 0.982. Besides, another linear relationship was observed with the equation $Y = 177*X + 67.9$ and R^2 value of 0.990, ranging from 0.1 μM to 0.1 mM. The limit of detection (LOD) was measured by 3.3 times the standard deviation obtained

6

from seven metrical values of the blank sample and the slope of the curve [43]. The LOD of SANs/GOx-coated SPE is calculated to be 0.059 µM at -0.22 V, which is lower than most of the reported enzymatic or non-enzymatic electrochemical glucose sensor in **Table S1**. For the practical application of glucose biosensors, anti-interference, reproducibility and stability are very crucial [44]. Glucose sensing is affected by other substances in the ISF [37, 45]. Therefore, the response current of various interfering substances and glucose at the same concentration was tested to investigate whether the interference would affect glucose detection. **Figure S5A** shows the ratio of the response current intensity of 5 mM interferences at -0.22 V using amperometry to the response current of glucose at 5 mM concentration. The response currents of the interferences are approximately 1% to 4% of glucose, indicating the response current generated by the interferences is insufficient to affect the accuracy of glucose detection. Therefore, the glucose biosensor can detect glucose in the presence of interferences in ISF. Figure S5B shows the response current of 2 mM glucose solution measured by seven electrodes fabricated by the same method. The standard deviation of the measured current was 2.55%, which means that the fabricated SANs/GOx-coated SPEs have good reproducibility. Figure S5C also shows the response current of 2 mM glucose solution from SANs/GOX-coated SPEs after 0, 7, 14, 21, 28 and 35 days of storage at room temperature. Most previously reported glucose sensors show significant performance degradation within 7 to 30 days of storage [44, 46-48]. However, SANs/GOx-coated SPEs proposed in this study were able to maintain about 94.5% current after 35 days of storage at room temperature, demonstrating the excellent stability after long-term storage.
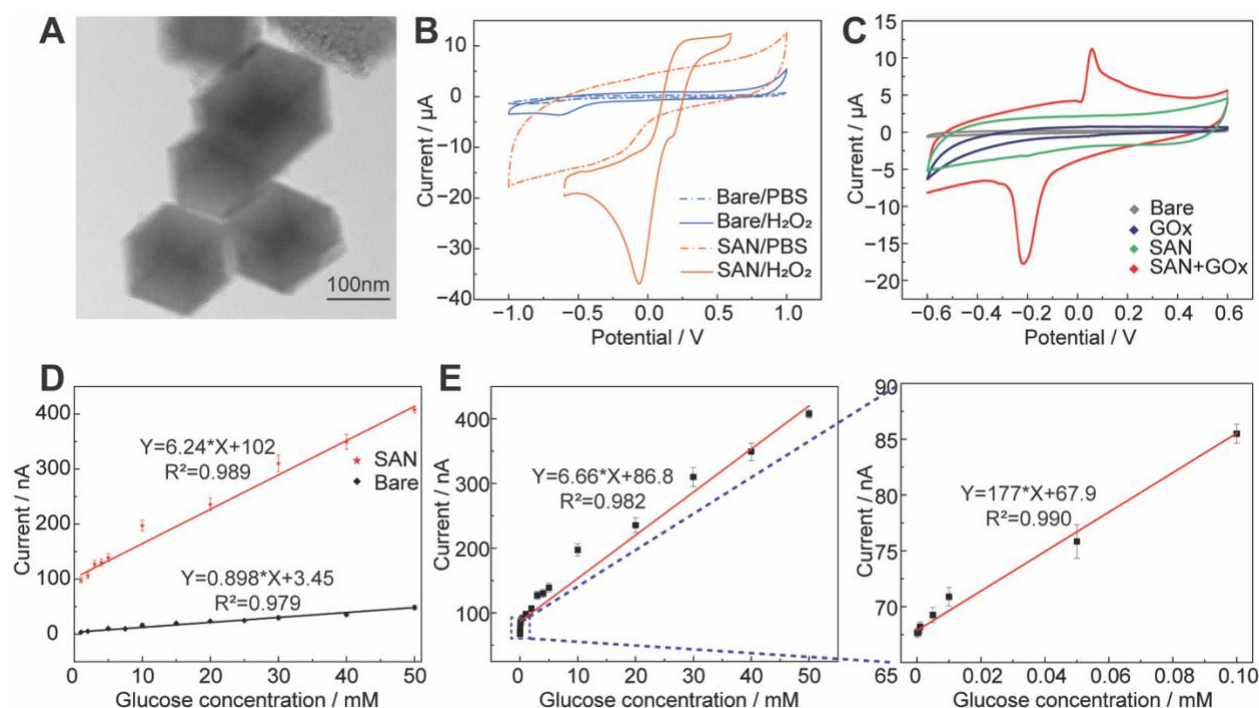
7

Figure 2. Characterization and detection performance of SANs. A) TEM image of SANs structure; B) CV curves of bare and SANs-coated SPE in PBS solution with or without 2.5 mM H_2O_2; C) CV curves of bare, GOx-coated, SANs-coated and SANs/GOx-coated SPE in 2.5 mM glucose solution; D) Comparison of glucose sensing performance of GOx-coated (black) and SANs/GOx-coated (red) SPE; E) The standard curve for glucose detection on SANs/GOx-coated SPE (Left detection range: from 0.1 mM to 50 mM; Right detection range: from 0.1 μM to 0.1 mM).

2.4 Fabrication and characterization of hollow microneedle patch

The microneedle array was fabricated by Anycubic SLA printer, which has a XY resolution of 16.8 × 24.8 μm. As shown in **Figure 3A**, the hollow microneedle array was composed of 5 × 5 HMN array (12 × 12 × 1.5 mm, L × W × H) with side openings (hole diameter of 0.16 mm) and through-microchannels (diameter of 0.6 mm). The base diameter, tip diameter, wall thickness and length of each HMN were 750 μm, 100 μm, 75 μm and 1000 μm, respectively. The center-to-center interspacing between HMN tips was optimized to 2 mm for optimal skin permeability and a reduction of insertion force [49-51]. For superior sharpness and dimensional accuracy, the HMN patch was printed with a 45° print angle along X and Y axes with the side opening of the HMNs

8

facing downward [52, 53]. The scanning electron microscopy (SEM) image, shown in **Figure 3A** depicts the morphology of the printed HMNs.

To visualize the stress distribution of the compression tests, a finite element analysis (FEA) of a single hollow microneedle was performed via Ansys 2024 R2 using the CAD model with a load force of 2 N on the tip surface. The estimated values of the resin parameters were 1150 kg/m^3 for density, 0.35 for Poisson's ratio, and 3.78×10^9 Pa for Young's modulus, respectively. The resultant equivalent von-Mises stress was depicted in **Figure 3B**, indicating that the highest stress concentration occurred at the tip of the microneedle (estimated around 2.14×10^8 Pa) and gradually decreased along the shaft [54].

Penetrating the stratum corneum of human skin requires a minimum insertion force of 0.08 N per needle [55]. To investigate the mechanical robustness, compression tests were conducted by applying a force of 50 N to evaluate their strength. The SEM image in **Figure 3C** suggested that no apparent deformation was observed after penetration tests, confirming that each needle can withstand at least 2 N without fracture. Under the given force load, the deformation was manifested towards the side with a hollow hole without any fracture, which was consistent with the FEA result. The recorded force-displacement curve for Samples 1-3 (**Figure 3D)** demonstrates that the whole compression process was kept in elastic region, assuring the HMNs did not fail during the compression experiments. The penetration performance and depth of HMNs were subsequently accessed on Samples 4-6 by parafilm penetration tests [56]. A force load was applied at a speed of 1 mm/min and removed when the resistance reached 40 N and held for 30 seconds [57]. The deformation resistance gradually decreased to approximately 25 N (**Figure 3E**). After the separation of HMNs, the SEM image (**Figure 3F**) of the HMNs and the optical images of parafilm layers (**Figure 3G**, from the 1st layer to the 6th layer) were captured. The penetration efficiency was analyzed according to the holes created on each parafilm layer and the results were shown in **Figure 3H**. It can be concluded that 82.67 ± 1.89 % of the fabricated HMNs were able to pierce about 3 layers of parafilm, affirming the successful penetration of HMNs to the dermis layer for ISF sampling [58]. Thus, the 3D-printed biocompatible HMNs demonstrated excellent mechanical stability and penetration performance for ISF sampling.
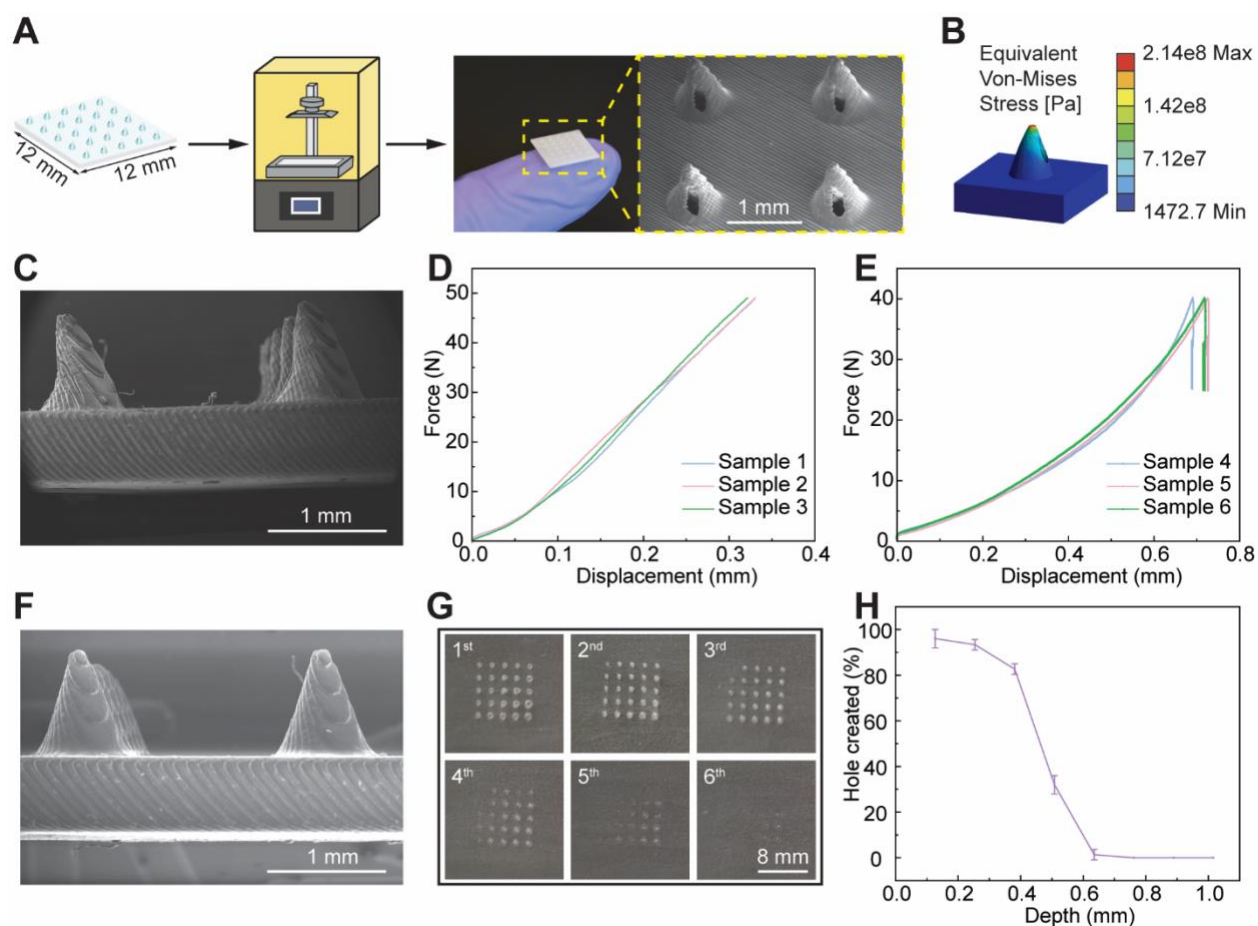
https://doi.org/10.26434/chemrxiv-2025-gv8xt ORCID: https://orcid.org/0000-0002-3138-0275 Content not peer-reviewed by ChemRxiv. License: CC BY 4.0

Figure 3. Fabrication and characterization of hollow microneedle patch. A) Fabrication process and SEM of HMNs; B) FEA of HMNs after compression; C) SEM of HMNs after compression test; D) Compression results of HMNs; E) Penetration results of parafilm penetration tests; F) SEM of HMNs after parafilm penetration tests; G) Optical photos of hole created on the parafilm (from the 1st layer to the 6th layer); H) Penetration efficiency of the HMNs on the parafilm.

2.5 Validation of the integrated sensor on skin-mimicking phantom gel in vitro

Glucose sensing was performed in simulated artificial ISF to verify the accuracy of the glucose detection using SANs/GOx-coated SPE. The ISF formula from previous studies was slightly modified to prepare artificial ISF for glucose sensing tests [59]. Parafilm and agarose hydrogel were used to mimic the human skin [27]. The schematic diagram of the detection of simulated skin ISF and optical image of detection device are shown in **Figure 4A**. The device includes a hollow microneedles array, a pump and SANs/GOx-coated SPE. **Figure 4B** illustrates the process for measuring glucose concentration in ISF within a skin-mimicking model. The hollow microneedles

10

penetrate the parafilm to absorb the ISF for glucose detection, with the pump providing negative pressure for ISF extraction. The SAN-coated SPE for glucose sensing is connected to wireless AC impedance/electrochemical impedance spectroscopy (EIS) potentiostat/EIWP110 to analyze the response current from SPE. **Figure 4C** shows the microneedles inserted into hydrogel and successfully extracted ISF. After the removal of the parafilm layer, the remaining holes in agarose hydrogel were shown in **Figure 4D,** demonstrating that the HMNs can pierce the parafilm layer and extract ISF from the gel. The response current was analyzed by EIS potentiostat and then the detection concentration of biomarker was rapidly wirelessly transmitted to and displayed on a smartphone app remotely, as shown in **Figure 4E**. Therefore, the detection method greatly reduces the time required to obtain glucose levels, allowing for a quick response. **Figure 4F** shows the curve of current and glucose concentration from the glucose sensor at different glucose concentrations in artificial ISF. The settings of EWIP110 software are shown in **Figure S6A** and the responding current curves are shown in **Figure S6B**. Within the detection range, a linear relationship between glucose concentration and response current was observed from 1 mM to 40 mM, following the equation of $Y = 0.0098*X + 0.0184$ and R^2 of 0.99. The curve was used as the standard curve for subsequent testing and entered the software, as shown in **Figure S6C**. The continuous detection curve for glucose in artificial ISF is shown in **Figure 4G**. The continuous increase in glucose concentration was achieved by adding higher concentrations of glucose ISF solution. The concentrations of glucose for continuous detection were 0.98, 5.08, 10.6 and 20.05 mM. Through the addition of glucose ISF solution, the response current increased rapidly and then the current value was stabilized. The results indicate that SANs coated-SPE electrochemical sensor can continuously and rapidly measure the glucose concentration in artificial ISF. **Figure 4H** shows the results of continuous detection of glucose in skin-mimicking model. The detection concentrations were 1, 2, 5, 10, 15 and 20 mM, respectively. As the increase of the glucose concentration in ISF, the response current increased continuously. When a time range was selected, the software would calculate the average current during this time and transfer current to concentration through the previously entered standard curve and transmitted it wirelessly on the smartphone app. Finally, the results from the proposed sensor were compared to the reference values of glucose concentration, as shown in **Table S2**. The glucose recoveries from artificial ISF and skin-mimicking phantom gel were approximately 102%-104% and 97%-105%, respectively. The recoveries demonstrate that the proposed sensor can accurately measure glucose concentration

11

in a simulated ISF environment. Compared to previous sensors with limited transmission distance, the proposed sensor achieves a reliable wireless range of 20m, providing greater mobility and flexibility to users. Therefore, the device combines SAN-coated SPE with an EIS potentiostat to achieve real-time and continuous glucose monitoring in ISF in a skin-mimicking model by changing the time range.
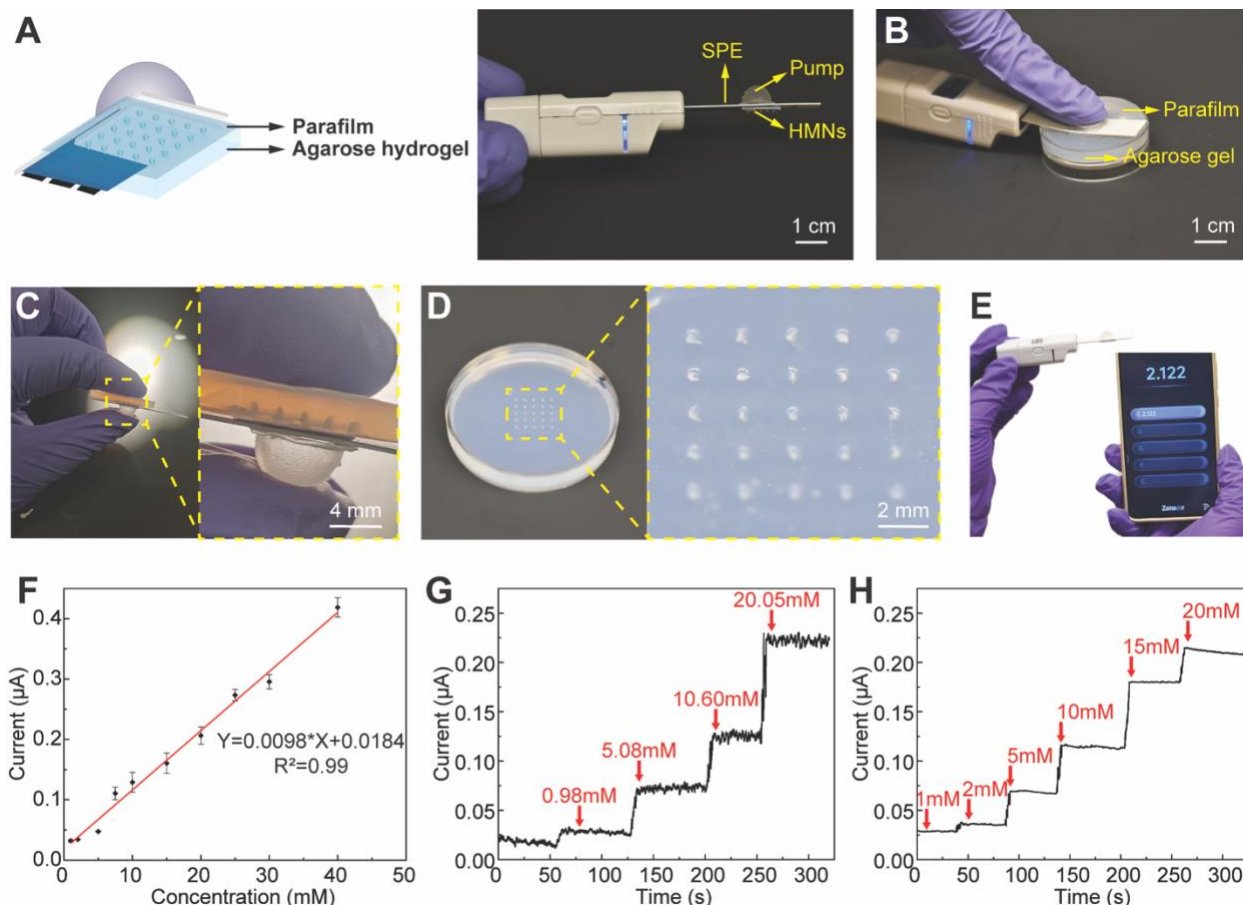

Figure 4. Glucose detection in artificial ISF and skin-mimicking phantom gel. A) Schematic diagram of glucose detection using SANs/GOx-coated SPE sensor in skin-mimicking phantom gel (Left) and assembly of the SANs/GOx-coated SPE sensor (Right); B) Glucose sensing operation process in skin-mimicking phantom gel; C) Microneedles array inserted into skin-mimicking phantom gel; D) Microwell array on gel in skin-mimicking phantom gel after detection E) The smartphone app used to display the glucose concentration measured by sensor; F) Standard curve of current and glucose concentration in artificial ISF using EIS potentiostat; G) Continuous curve of current and time from sensing glucose in artificial ISF using EIS potentiostat; H) Continuous

12

curve of current and time from sensing glucose in skin-mimicking phantom gel using EIS potentiostat.

3. Conclusion

This study successfully demonstrated a biocompatible, SANs-functionalized, 3D-printed hollow microneedle-based electrochemical sensor for wireless, continuous and real-time glucose monitoring in interstitial fluid. The integration of biocompatible HMNs and a finger-activated pump exhibits the potential for minimally invasive sampling of ISF. The SANs-boosted electrochemical sensor highlighted high sensitivity and remarkable selectivity, while the wireless potentiostat enabled user-friendly, real-time and continuous monitoring of glucose levels. In the proof-of-concept, a skin-mimicking phantom gel was used to validate the electrochemical sensing capability and sensitivity *"in vivo"*. Our integrated wearable sensor provides a feasible solution for continuous and precise glucose monitoring, representing the potential for health monitoring. Future studies will focus on refining the fabrication techniques to develop miniaturized devices and optimizing material properties for enhanced sensing performance. Additionally, we aim to expand our device's capabilities to monitor multiple biomarkers for comprehensive health management. With these advancements, we believe our proposed work is promising to notably contribute to the development of the next-generation wearable devices, paving the way for personalized healthcare.

4. Experimental Section

4.1 Fabrication of HMNs and Pump by Resin 3D Printers

HMNs (5 × 5 array) and elastic pump were fabricated using Anycubic bio resin on a resin 3D printer (Anycubic Photon Mono M5s Pro, *Anycubic Technology Co*., Shenzhen, China) and Elastic 50A Resin V2 (Form 3) on Form 3+ printer (Formlab, Somerville, MA, USA), respectively. The microneedle arrays and pump were designed in AutoCAD software (Fusion 360, Autodesk, USA) and exported to .STL format files. The HMN model files were subsequently rotated by 45 degrees along both the X and Y axes for optimized supports and sliced using Anycubic Photon Workshop software, while the pump was auto-oriented and sliced by PreForm software. After the 3D printing process completed, the prints were removed from the build platform and cleaned with an isopropyl

https://doi.org/10.26434/chemrxiv-2025-gv8xt **ORCID:** https://orcid.org/0000-0002-3138-0275 Content not peer-reviewed by ChemRxiv. **License:** CC BY 4.0

alcohol solution to wash off residual resin. These prints were post-cured in a UV cure machine (λ = 405 nm) for solidification, followed by removal of model supports.

4.2 Morphology Characterization of HMNs

HMNs were coated with 10 nm thick gold and characterized using scanning electron microscopy (FEI SEM Apreo Volumescope). SEM imaging of the HMNs was used to image the morphology of the HMNs after fabrication and the microneedle tip deformation during compression and parafilm penetration tests.

4.3 Mechanical and Penetration Characterization of HMNs

The compression tests and parafilm penetration tests were performed on an Instron universal testing machine (Instron, model 600DX-C4A-G7G, Canton, MA, USA). The compression tests were used to examine the mechanical strength and the parafilm penetration tests were used to evaluate the penetration efficiency of the 3D-printed HMNs [56]. HMN patches were placed on the test platform with the tips upward, and a vertical force was applied at a moving speed of 1 mm/min. The loading force against displacement data was recorded during the test until the maximum force of 50N was reached. For the parafilm penetration tests, HMN patches were placed on the top of the eight-layer parafilm (127 µm thickness per sheet) with the tip facing down, and the vertical force was applied to the HMNs at a load rate of 1 mm/min. When the loading force reached at 40 N, the ramp speed was reduced to 0 mm/min and the force was maintained for 30 seconds [57]. After that, the HMNs were removed and the parafilm sheets were separated to count the holes created on each layer. These mechanical tests were repeated 3 times. The penetration efficiency was calculated according to the ratio of holes generated in each layer using the following equation [60]:

$$\text{Hole created (\%)} = (\text{Number of holes observed} / \text{Number of HMN}) \times 100.$$

4.4 Preparation of Fe-N-C SANs

The preparation of Fe-N-C SANs was based on our previous reports [36]. 100 mg of $Fe(NO_3)_3 \cdot 9H_2O$ was introduced into 160 mL of methyl alcohol containing 3.39 mg of $Zn(NO_3)_2 \cdot 6H_2O$ with intense ultrasound for 30 minutes. Following this, another 160 mL of methyl alcohol solution containing 3.94 g of 2-Methylimidazole (2-MeIM) was added to the above solution. Then, the above mixture

14

was sealed in an Erlenmeyer flask, shaken for 1 minute and allowed to stand overnight at 60 °C. The Fe-doped ZIF-8 was collected after centrifugation at 7000 rpm (Eppendorf Centrifuge 5804 R, German) for 10 minutes and washed three times with deionized water and ethyl alcohol respectively. Fe-N-C SANSANs were obtained from a pyrolytic process of the Fe-doped ZIF-8 at 900 °C (Across International STF 1200 Tube Furnace, USA) under a nitrogen atmosphere for 30 minutes, followed by an ammonia atmosphere for 30 minutes. Fe-N-C SANs were washed with 2 mol/L of HCl at 60 °C for 6 h. Finally, the Fe-N-C SANs were dried in freeze dryer (FreeZone 4.5 Liter-50C Benchtop Freeze Dryer) and stored away from light for later use.

4.5 Characterization of Fe-N-C SANs

The morphology and structure of Fe-N-C SANs were performed using transmission electron microscopy (FEI Tecnai G2 20 Twin TEM, 200 kV LaB6 electron source). Electrochemical analysis was performed by CV and amperometry method with a CHI660E series electrochemical workstation (CH Instruments, Inc. Austin, USA). 4uL of ink was dropped onto the surface of SPE and the electrode was dried at room temperature. The bare SPE was immersed in 100 mL 0.01 M PBS containing 0 and 2.5 mM H_2O_2 for electrochemical analysis using CV. Similarly, 100 mL of 0.01 M PBS containing 0, 2.5, 5, and 7.5 mM H_2O_2 was measured by SANs-coated SPE by CV. The CV measurements were conducted at a scan speed of 50 mV/s. The amperometry method was used to analyze the response of SANs-coated SPE to varying concentrations of H_2O_2. Amperometry measurement was performed at -0.1 V using the SPE. The SANs-coated SPE was immersed in 100 mL of stirred 0.01 M PBS solution. 50 uL of 200 mM H_2O_2 (in PBS) was added to the solution each time, and the corresponding current change over time was obtained using amperometry.

4.6 Preparation and detection performance of Fe-N-C SANs-coated screen-printed electrode

SPE was activated using CV with a potential range of -2.5 V to 2.5 V and a sweep rate of 100 mV/s over 3 segments. 5 mg of Fe-N-C SANs were dissolved in a mixture solution containing 990 μL PBS and 10 μL 1 wt% Nafion to prepare a 5 mg/mL ink. Then, 4 μL of ink was dropped onto the WE surface of the SPE. After drying at room temperature, the SANs-coated SPE was obtained. SANs-coated SPE was then immersed in 2 mg/mL of GOx solution for 24 hours to obtain SAN/Gox-coated SPE. Meanwhile, an SPE without SANs was also immersed in 2 mg/mL of Gox

15

for 24 hours to obtain a GOx-coated SPE. The CV method was conducted to evaluate the electrochemical properties of modified SPEs. The CV settings were the same as in section **2.5**. Bare SPE, GOx-coated SPE and SANs/GOx-coated SPE were analyzed in a 2.5 mM glucose solution using CV with the CHI660E electrochemical workstation. The SANs-coated SPE was measured in 0.01 M PBS using the same method. The amperometry method was applied for glucose detection at -0.22 V via CHI660E electrochemical workstation. D-glucose was dissolved in 0.01 M PBS (pH 7.4) to prepare glucose solutions with a concentration range of 0.1 μM to 40 mM for the calibration curve. 70 uL of glucose solutions were dropped onto the three electrodes of SANs/GOx-coated SPE and GOx-coated SPE respectively to obtain the response currents to varying glucose concentrations at -0.22 V. Then, 5 mM uric acid, L-alanine, lactate, and ascorbic acid were prepared for interference test. 70 uL of interference solutions were added onto the electrodes of SANs/GOx-coated SPE to analyze the response current using amperometry at -0.22 V. Seven identical SAN/GOx coated SPEs were made using the same method and then tested with 2 mM glucose solution using amperometry. Meanwhile, the SAN/GOx coated SPEs were stored at 4 °C and room temperature for one month and tested with 1 mM glucose solution using amperometry every week.

4.7 Glucose detection in artificial interstitial fluid

To prepare artificial ISF, 2.5 mM $CaCl_2$, 5.5 mM glucose, 10 mM HEPES, 3.5 mM KCl, 0.7 mM $MgSO_4$, 123 mM NaCl, 1.5 mM NaH_2PO_4, and 7.4 mM saccharose were dissolved in Milli-Q water and the pH was adjusted to 7.0 using HCl solution [59, 61, 62]. All chemicals were used without further modification and purification. Glucose detection in artificial ISF was conducted by ECWP110plus wireless potentiostat (Zensor R&D co., Ltd). The potentiostat device consists of a remoter and a connector. SANs/GOx-coated SPE was inserted into the connector, while the remoter was connected to the USB port of a computer. The connector collected the electric signal from SPE and transmitted the signal to computer via the remoter. Amperometric method was applied to analyze the signal from connector in EIWP110 software (Zensor R&D co., Ltd) on computer. The operation interface is displayed in **Figure S6**. As shown in **Figure S6A** and **B**, the potential was set to -0.22V to obtain the response currents which were obtained to create the standard curve correlating current with glucose concentration in ISF. In **Figure S6C**, the standard curve equation was entered into software for subsequent detection. The above method was also

16

applied to continuous glucose detection in ISF. To perform continuous detection, the glucose ISF solution was added to the ISF solution to achieve a continuous increase in the ISF solution. During the continuous measurement, concentrations of glucose were 0.98, 5.98, 10.60 and 20.05 mM, respectively. After adding glucose solution in artificial ISF, the magnetic bead was constantly stirred in the ISF solution to quickly reach the target glucose concentration. After analysis by EIWP110 software, the amperometry curve was shown. The concentration would be calculated using the formula that has been entered and displayed on the software interface. Meanwhile, the results were sent wirelessly and displayed on the smartphone app, ECWP (Zensor R&D co., Ltd).

4.8 *In Vivo* Evaluation in Skin-Mimicking Phantom Gel

To simulate the mechanical properties of human skin, a skin-mimicking phantom gel was prepared and used to evaluate the electrochemical performance of the sensor [63]. A 1.4% agarose gel was prepared by mixing 140 mg of agarose into 10 mL of the aforementioned artificial ISF. The mixture was continuously stirred at 120 °C until it became completely clear. Subsequently, the solution was poured into round-shape molds to solidify at room temperature. To further mimic skin, a layer of parafilm was placed over the prepared gel [27]. During the "i*n vivo"* phantom hydrogel experiments, the HMNs of the sensor were penetrated through the parafilm into the phantom gel, The HMNs remained in contact with the gel for 1 minute before the electrochemical detection of the glucose [64]. This setup verified the ISF sampling ability and the electrochemical sensitivity of the integrated sensor. The same method used for glucose detection in ISF was applied to detect glucose concentration in skin-mimicking phantom gel. The signal from connector was analyzed using amperometry in the EIWP110 software. Once the current stabilized, the gel with a certain concentration of glucose was replaced with the gel containing a different glucose concentration. Glucose ISF solutions of 1, 2, 5, 10, 15 and 20 mM were detected continuously. The result was sent to smartphone app after the analysis of software using amperometry.

Acknowledgments

Conflict of Interest

The authors declare no conflict of interest.

References

[1]   Kharroubi, A. T.; Darwish, H. M., *World J. Diabetes* **2015,** *6* (6), 850.

[2]   Mukhtar, Y.; Galalain, A.; Yunusa, U., *European Journal of Biology* **2020,** *5* (2), 1-14.

[3]   Eivazzadeh-Keihan, R.; Bahojb Noruzi, E.; Chidar, E.; Jafari, M.; Davoodi, F.; Kashtiaray, A.; Ghafori Gorab, M.; Masoud Hashemi, S.; Javanshir, S.; Ahangari Cohan, R.; Maleki, A.; Mahdavi, M., *Chemical Engineering Journal* **2022,** *442*, 136183.

[4]   Lee, I.; Probst, D.; Klonoff, D.; Sode, K., *Biosens. Bioelectron.* **2021,** *181*, 113054.

[5]   Klonoff, D. C.; Ahn, D.; Drincic, A., *Diabetes Res. Clin. Pract.* **2017,** *133*, 178-192.

[6]   Rodbard, D., *Diabetes Technol. Ther.* **2016,** *18* (S2), S2-3.

[7]   Tierney, M. J.; Tamada, J. A.; Potts, R. O.; Jovanovic, L.; Garg, S., *Biosens. Bioelectron.* **2001,** *16* (9), 621-629.

[8]   Wu, J.; Liu, Y.; Yin, H.; Guo, M., *Am J Transl Res* **2023,** *15* (6), 3825-3837.

[9]   Zou, Y.; Chu, Z.; Guo, J.; Liu, S.; Ma, X.; Guo, J., *Biosensors and Bioelectronics* **2023,** *225*, 115103.

[10]   Jernelv, I. L.; Milenko, K.; Fuglerud, S. S.; Hjelme, D. R.; Ellingsen, R.; Aksnes, A., *Applied Spectroscopy Reviews* **2019,** *54* (7), 543-572.

[11]   Ahmed, I.; Jiang, N.; Shao, X.; Elsherif, M.; Alam, F.; Salih, A.; Butt, H.; K. Yetisen, A., *Sensors & Diagnostics* **2022,** *1* (6), 1098-1125.

[12]   Pu, Z.; Zhang, X.; Yu, H.; Tu, J.; Chen, H.; Liu, Y.; Su, X.; Wang, R.; Zhang, L.; Li, D., *Science Advances* **2021,** *7* (5), eabd0199.

[13]   Wang, H.; Yao, C.; Liu, Z.; Wang, X.; Liu, Z.; Zhang, T.; Huang, X.; Wang, L.; Wang, Y.; Xiao, G.; Farah, S.; Chen, H.-j.; Xie, X., *Advanced Intelligent Systems* **2024,** *n/a* (n/a), 2400547.

[14]   Dervisevic, M.; Alba, M.; Yan, L.; Senel, M.; Gengenbach, T. R.; Prieto-Simon, B.; Voelcker, N. H., *Advanced Functional Materials* **2022,** *32* (3), 2009850.

[15]   Parrilla, M.; Detamornrat, U.; Domínguez-Robles, J.; Donnelly, R. F.; De Wael, K., *Talanta* **2022,** *249*, 123695.

[16]   Jain, P.; Joshi, A. M.; Mohanty, S. P.; Cenkeramaddi, L. R., *IEEE Access* **2024,** *12*, 61907-61936.

[17]   Heikenfeld, J.; Jajack, A.; Feldman, B.; Granger, S. W.; Gaitonde, S.; Begtrup, G.; Katchman, B. A., *Nat. Biotechnol.* **2019,** *37* (4), 407-419.

[18]   Tang, L.; Chang, S. J.; Chen, C.-J.; Liu, J.-T., *Sensors* **2020,** *20* (23), 6925.

[19]   García-Guzmán, J. J.; Pérez-Ràfols, C.; Cuartero, M.; Crespo, G. A., *TrAC, Trends Anal. Chem.* **2021,** *135*, 116148.

[20]   Friedel, M.; Thompson, I. A. P.; Kasting, G.; Polsky, R.; Cunningham, D.; Soh, H. T.; Heikenfeld, J., *Nat. Biomed. Eng* **2023,** *7* (12), 1541-1555.

[21]   Teymourian, H.; Tehrani, F.; Mahato, K.; Wang, J., *Advanced healthcare materials* **2021,** *10* (17), 2002255.

[22]   Abbasiasl, T.; Mirlou, F.; Mirzajani, H.; Bathaei, M. J.; Istif, E.; Shomalizadeh, N.; Cebecioğlu, R. E.; Özkahraman, E. E.; Yener, U. C.; Beker, L., *Adv. Mater.* **2024,** *36* (2), 2304704.

[23]   Bao, L.; Park, J.; Bonfante, G.; Kim, B., *Drug Delivery LettersDrug Delivery and Translational Research* **2022,** *12* (2), 395-414.

[24]   Lee, K.; Goudie, M. J.; Tebon, P.; Sun, W.; Luo, Z.; Lee, J.; Zhang, S.; Fetah, K.; Kim, H.-J.; Xue, Y.; Darabi, M. A.; Ahadian, S.; Sarikhani, E.; Ryu, W.; Gu, Z.; Weiss, P. S.; Dokmeci, M. R.; Ashammakhi, N.; Khademhosseini, A., *Adv. Drug Del. Rev.* **2020,** *165-166*, 41-59.

[25]   Jamaledin, R.; Yiu, C. K. Y.; Zare, E. N.; Niu, L.-N.; Vecchione, R.; Chen, G.; Gu, Z.; Tay, F. R.; Makvandi, P., *Adv. Mater.* **2020,** *32* (33), 2002129.

[26]   Liu, Y.; Yu, Q.; Luo, X.; Yang, L.; Cui, Y., *Microsyst. Nanoeng.* **2021,** *7* (1), 1-12.

[27]   Teymourian, H.; Moonla, C.; Tehrani, F.; Vargas, E.; Aghavali, R.; Barfidokht, A.; Tangkuaram, T.; Mercier, P. P.; Dassau, E.; Wang, J., *Anal. Chem.* **2020,** *92* (2), 2291-2300.

[28]   Jiang, X.; Wilkirson, E. C.; Bailey, A. O.; Russell, W. K.; Lillehoj, P. B., *Cell Rep. Phys. Sci.* **2024,** *5* (6).

[29]   Samant, P. P.; Niedzwiecki, M. M.; Raviele, N.; Tran, V.; Mena-Lapaix, J.; Walker, D. I.; Felner, E. I.; Jones, D. P.; Miller, G. W.; Prausnitz, M. R., *Sci. Transl. Med.* **2020,** *12* (571), eaaw0285.

[30]   Jiao, L.; Yan, H.; Wu, Y.; Gu, W.; Zhu, C.; Du, D.; Lin, Y., *Angewandte Chemie* **2020,** *132* (7), 2585-2596.

[31]   Cheng, N.; Li, J.-C.; Liu, D.; Lin, Y.; Du, D., *Small* **2019,** *15* (48), 1901485.

[32]   Ding, S.; Barr, J. A.; Lyu, Z.; Zhang, F.; Wang, M.; Tieu, P.; Li, X.; Engelhard, M. H.; Feng, Z.; Beckman, S. P.; Pan, X.; Li, J.-C.; Du, D.; Lin, Y., *Advanced Materials* **2024,** *36* (10), 2209633.

[33]   Chen, C.; Fu, Y.; Sparks, S. S.; Lyu, Z.; Pradhan, A.; Ding, S.; Boddeti, N.; Liu, Y.; Lin, Y.; Du, D.; Qiu, K., *ACS Sens.* **2024,** *9* (6), 3212-3223.

[34]   Lyu, Z.; Ding, S.; Tieu, P.; Fang, L.; Li, X.; Li, T.; Pan, X.; Engelhard, M. H.; Ruan, X.; Du, D.; Li, S.; Lin, Y., *Research* **2022,** *2022*.

[35]   Niu, X.; Shi, Q.; Zhu, W.; Liu, D.; Tian, H.; Fu, S.; Cheng, N.; Li, S.; Smith, J. N.; Du, D.; Lin, Y., *Biosensors and Bioelectronics* **2019,** *142*, 111495.

[36]   Fu, S.; Zhu, C.; Su, D.; Song, J.; Yao, S.; Feng, S.; Engelhard, M. H.; Du, D.; Lin, Y., *Small* **2018,** *14* (12), 1703118.

[37]   Ayankojo, A. G.; Reut, J.; Ciocan, V.; Öpik, A.; Syritski, V., *Talanta* **2020,** *209*, 120502.

[38]   Ding, S.; Lyu, Z.; Li, S.; Ruan, X.; Fei, M.; Zhou, Y.; Niu, X.; Zhu, W.; Du, D.; Lin, Y., *Biosensors and Bioelectronics* **2021,** *191*, 113434.

[39]   Khatami, S. H.; Vakili, O.; Ahmadi, N.; Soltani Fard, E.; Mousavi, P.; Khalvati, B.; Maleksabet, A.; Savardashtaki, A.; Taheri-Anganeh, M.; Movahedpour, A., *Biotechnology and Applied Biochemistry* **2022,** *69* (3), 939-950.

[40]   Jiao, L.; Xu, W.; Yan, H.; Wu, Y.; Liu, C.; Du, D.; Lin, Y.; Zhu, C., *Analytical Chemistry* **2019,** *91* (18), 11994-11999.

[41]   Lyu, Z.; Ding, S.; Zhang, N.; Zhou, Y.; Cheng, N.; Wang, M.; Xu, M.; Feng, Z.; Niu, X.; Cheng, Y.; Zhang, C.; Du, D.; Lin, Y., *Research* **2020,** *2020*.

[42]   Niu, X.; Li, X.; Lyu, Z.; Pan, J.; Ding, S.; Ruan, X.; Zhu, W.; Du, D.; Lin, Y., *Chemical Communications* **2020,** *56* (77), 11338-11353.

[43]   Müsse, A.; La Malfa, F.; Brunetti, V.; Rizzi, F.; De Vittorio, M., *Micromachines* **2021,** *12* (7), 805.

[44]   Xu, Z.; Wang, Q.; Zhangsun, H.; Zhao, S.; Zhao, Y.; Wang, L., *Food Chemistry* **2021,** *349*, 129202.

[45]   Yao, Y.; Chen, J.; Guo, Y.; Lv, T.; Chen, Z.; Li, N.; Cao, S.; Chen, B.; Chen, T., *Biosensors and Bioelectronics* **2021,** *179*, 113078.

[46]   Gopal, T. S.; Jeong, S. K.; Alrebdi, T. A.; Pandiaraj, S.; Alodhayb, A.; Muthuramamoorthy, M.; Andrews Nirmala, G., *Materials Today Chemistry* **2022,** *24*, 100891.

[47]   Kong, C.; Tang, L.; Zhang, X.; Sun, S.; Yang, S.; Song, X.; Yang, Z., *Journal of Materials Chemistry A* **2014,** *2* (20), 7306-7312.

[48]   Gou, X.; Sun, S.; Yang, Q.; Li, P.; Liang, S.; Zhang, X.; Yang, Z., *New Journal of Chemistry* **2018,** *42* (8), 6364-6369.

[49]   Ebrahiminejad, V.; Prewett, P. D.; Davies, G. J.; Faraji Rad, Z., *Adv. Mater. Interfaces* **2022,** *9* (6), 2101856.

[50]   Lori Zoudani, E.; Nguyen, N.-T.; Kashaninejad, N., *Small Struct.*, 2400121.

[51]   Xenikakis, I.; Tsongas, K.; Tzimtzimis, E. K.; Katsamenis, O. L.; Demiri, E.; Zacharis, C. K.; Georgiou, D.; Kalogianni, E. P.; Tzetzis, D.; Fatouros, D. G., *J. Drug Deliv. Sci. Technol.* **2022,** *67*, 102891.

[52]   Loh, J. M.; Lim, Y. J. L.; Tay, J. T.; Cheng, H. M.; Tey, H. L.; Liang, K., *Bioactive Materials* **2024,** *32*, 222-241.

[53]   Razzaghi, M.; Ninan, J. A.; Azimzadeh, M.; Askari, E.; Najafabadi, A. H.; Khademhosseini, A.; Akbari, M., *Adv. Healthc. Mater.* **2024,** *13* (23), 2400881.

[54]   Yeung, C.; Chen, S.; King, B.; Lin, H.; King, K.; Akhtar, F.; Diaz, G.; Wang, B.; Zhu, J.; Sun, W.; Khademhosseini, A.; Emaminejad, S., *Biomicrofluidics* **2019,** *13* (6), 064125.

[55]   Davis, S. P.; Landis, B. J.; Adams, Z. H.; Allen, M. G.; Prausnitz, M. R., *J. Biomech.* **2004,** *37* (8), 1155-1163.

[56]   Alrimawi, B. H.; Yi Lee, J.; Wooi Ng, K.; Fu Goh, C., *RSC Pharmaceutics* **2024,** *1* (2), 227-233.

[57]   Larrañeta, E.; Moore, J.; Vicente-Pérez, E. M.; González-Vázquez, P.; Lutton, R.; Woolfson, A. D.; Donnelly, R. F., *Int. J. Pharm.* **2014,** *472* (1), 65-73.

[58]   Zhang, X.; Zhang, W.; Wu, W.; Chen, J., *Microchem. J.* **2023,** *195*, 109477.

[59]   Bollella, P.; Sharma, S.; Cass, A. E. G.; Antiochia, R., *Electroanalysis* **2019,** *31* (2), 374-382.

[60]   Sabri, A. H.; Cater, Z.; Ogilvie, J.; Scurr, D. J.; Marlow, M.; Segal, J., *J. Drug Deliv. Sci. Technol.* **2020,** *58*, 101766.

[61]   Bretag, A. H., *Life Sci.* **1969,** *8* (5, Part 1), 319-329.

[62]   Chinnadayyala, S. R.; park, J.; Satti, A. T.; Kim, D.; Cho, S., *Electrochim. Acta* **2021,** *369*, 137691.

[63]   Tawakey, S. H.; Mansour, M.; Soltan, A.; Salim, A. I., *Lab Chip* **2024,** *24* (16), 3958-3972.

[64]   Goud, K. Y.; Mahato, K.; Teymourian, H.; Longardner, K.; Litvan, I.; Wang, J., *Sens. Actuator B-Chem.* **2022,** *354*, 131234.

TOC
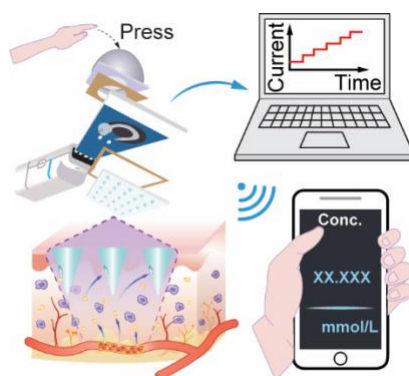
Chuchu Chen, Yonghao Fu, and co-workers present a novel wearable electrochemical sensor combining 3D-printed hollow microneedle array, a finger-activated pump, and single-atom nanozymes for highly sensitive glucose monitoring. This versatile platform enabled minimally invasive artificial interstitial fluid extraction and wireless real-time data transmission to a smartphone app, highlighting its potential for point-of-care health monitoring.